3D Shaping of a Focused Aperture in the Near Field

Ioannis Iliopoulos, Massimiliano Casaletti, Ronan Sauleau, Philippe Pouliguen, Patrick Potier, Mauro Ettorre

3-D Shaping of a Focused Aperture in the Near Field

Ioannis Iliopoulos, *Student Member, IEEE*, Massimiliano Casaletti, *Member, IEEE*, Ronan Sauleau, *Senior Member, IEEE*, Philippe Pouliguen, Patrick Potier, and Mauro Ettorre, *Senior Member, IEEE*

***Abstract*— The manipulation of the near-field (NF) is a challenging topic in electromagnetics, carrying essential importance for several applications. In this paper, we develop an algorithm capable of shaping the NF in 3-D domains according to given specifications. The algorithm is based on a set theoretic approach and a front-and-back iterative propagation scheme. The latter is realized using fast Fourier transforms (FFT), reducing the required computational time. The algorithm is applied on a focal shaping scenario. In this case, a full control of the depth of focus, spot diameter, and sidelobe level of the generated radiation is achieved. In particular, the proposed procedure is successfully adopted to control the normal component of a radiating aperture over a range of 12λ at 30 GHz. The derived aperture field distribution is then synthesized by a radial line slot antenna (RLSA) by means of an in-house method of moments (MoM) code. NF measurements have validated the proposed approach and prototype.**

***Index Terms*— 3-D near-field (NF) shaping, aperture antennas, focal systems, millimeter waves, slot antennas.**

I. Introduction

THE engineering of the near-field (NF) of a radiating system is becoming an interesting research field due to the numerous applications, ranging from NF radiometry [1] to deep tissue hyperthermia [2] and power transfer to implants [3]. In general, the goal is to achieve a specific field pattern, in the vicinity of an antenna, either in free space or inside specific media. However, in contrast with standard far-field techniques in antenna applications, there are no well-established design rules to follow.

The method proposed in [4] is generally used to design NF focusing antennas by opportunely using an equivalence between the far and Fresnel zone fields generated by a planar radiating aperture [5]. This approach lacks precision in predicting the focal characteristics in microwave or millimeter wave applications, due to the relatively small radiating apertures, as described in-depth in [6]. The authors of [7] and [8] have recently proposed a ray approach to design NF focusing systems using leaky-wave antennas. In this case, the leaky-wave mode is tailored along the radiating aperture, so that each point on the aperture radiates at a specific location in space. Various prototypes have been designed to prove the concept.

Nevertheless, all these examples suffer from one main problem: the focal characteristics cannot be controlled *a priori*. This means that the focal spot generated by the aperture, in terms of its figures of merit (FoMs), namely, spot diameter or beamwidth, depth of focus (DoF) (distance of -3 dB points of the field intensity in the direction normal to the radiating aperture) and sidelobe level (SLL), cannot be predefined at the beginning of the design process. Only in [9], some FoMs are partially associated with the polarization and the amplitude distribution of the radiating aperture, while a relevant work in optics can be found in [10].

The first work achieving full control over the spot diameter and the SLL has been described in [11], where an iterative algorithm is forcing the radiated field within a specific mask defined by the user. The aforementioned technique can support only 2-D shaping, meaning that the field can be shaped only over one plane parallel to the aperture, without any control of the generated field outside this region.

An important line of work can be found at optical frequencies. There, the nature of the sources, with sizes of thousands of λ's (an equivalent aperture at millimeter waves would measure some meters), gives plenty of freedom in shaping the field even in 3-D domains. An excellent example of 3-D shaping at optical frequencies can be found in [12], while exceptional interest present the so-called "Frozen Waves" [13]–[15].

An impressive methodology to shape the NF has been proposed in [16], where an almost automatic retunable system is considered. However, this system uses multiple transducers, which complicates the required feeding network for practical applications.

In this paper, we propose 3-D control of the radiated NF at millimeter waves. A theoretical methodology is described, and the results are validated by simulations and measurements of a successful prototype. The theoretical methodology is based on set theoretic approach and a projection method technique. The

I. Iliopoulos, R. Sauleau, and M. Ettorre are with the Institut d'Electronique et de Télecommunications de Rennes (IETR, UMR CNRS 6164), Université de Rennes 1, 35042 Rennes, France (e-mail: ioannis.iliopoulos@univ-rennes1.fr).

M. Casaletti is with the Sorbonne Universités, University Pierre and Marie Curie Paris 06, Unité de Recherche 2 (UR2), Laboratoire d'Electronique et Electromagnétisme (L2E), F-75005 Paris, France (e-mail: massimiliano.casaletti@upmc.fr).

P. Pouliguen is with the Strategy Directorate, Direction Générale de l'Armement, 75509 Paris, France (e-mail: philippe.pouliguen@intradef.gouv.fr).

P. Potier is with the Information Superiority, Direction Générale de l'Armement, 35170 Bruz, France (e-mail: patrick.potier@intradef.gouv.fr).

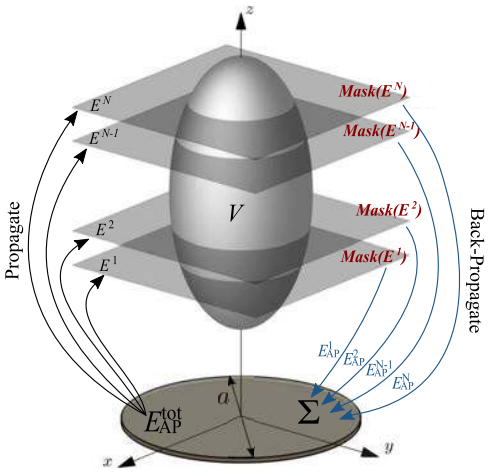

Fig. 1. Problem setup with an illustration of the applied algorithm.

practical part (i.e., the antenna design) is facilitated by an in-house MoM tool. To the authors' best knowledge, it is the first time that the NF of a radiating aperture has been controlled over a 3-D domain.

This paper is structured as follows. Section II is devoted to setting-up the considered problem. The proposed iterative algorithm is presented and specialized in focusing in 3-D domains. Section III presents the design of a radial line slot antenna (RLSA), synthesizing the required aperture field profile. Section IV is dedicated to prototyping and measurements. Finally, Section V concludes the work.

II. 3-D Near-Field Shaping

3-D NF shaping consists in engineering the electromagnetic field close to a given radiating structure. Thus, the problem consists in defining the source distribution that yields the requested field shape in a predefined volume V (Fig. 1). Ultimately, the goal is to shape the norm of the field, which comprises the three field components in the form of [12]

$$I = \sqrt{|E_x|^2 + |E_y|^2 + |E_z|^2}. \tag{1}$$

It is apparent that this is a vectorial problem that presents great complication when addressed. A possible simplification is obtained by forcing a specific polarization to the radiated field. For example, a radial field polarization (i.e., $E_x = E_\rho \cos\phi$, $E_y = E_\rho \sin\phi$) can reduce the problem to $I = \sqrt{|E_\rho|^2 + |E_z|^2}$, while other assumptions (e.g., choice of antenna topology) could further simplify the problem.

However, in the case of planar radiating structures, the decomposition of the field in transverse electric (TE) and transverse magnetic (TM) modes (with respect to the normal direction to the aperture plane) can be used to reduce the complexity of the problem by reshaping it into a scalar form. Without loss of generality, and in order to facilitate the analysis, let us assume that our setup supports only a TM mode generated by an aperture situated at the xy-plane (Fig. 1). In such a problem, the field can be expressed in terms of a magnetic vector potential $\mathbf{A}$. It can be shown [17] that, for the geometry under consideration, only the scalar A_z component of the potential is sufficient for deriving the vector field.

Under these assumptions, the electric field components in a source-free region inside a medium with permittivity ε and permeability μ write [18]

$$E_x = -j\frac{1}{\omega\mu\varepsilon}\frac{\partial^2 A_z}{\partial x \partial z} \tag{2a}$$

$$E_y = -j\frac{1}{\omega\mu\varepsilon}\frac{\partial^2 A_z}{\partial y \partial z} \tag{2b}$$

$$E_z = -j\frac{1}{\omega\mu\varepsilon}\left(\frac{\partial^2}{\partial z^2} + k^2\right) A_z \tag{2c}$$

where ω is the angular frequency and k is the wavenumber inside the medium. Supposing a dependence of A_z over z in $e^{-jk_z z}$, where we have considered the separation relation

$$k^2 = k_x^2 + k_y^2 + k_z^2 \tag{3}$$

and (2) simplifies into

$$E_x = -\eta\frac{k_z}{k}\frac{1}{\mu}\frac{\partial A_z}{\partial x} \tag{4a}$$

$$E_y = -\eta\frac{k_z}{k}\frac{1}{\mu}\frac{\partial A_z}{\partial y} \tag{4b}$$

$$E_z = j\eta\frac{k^2 - k_z^2}{k}\frac{1}{\mu}A_z \tag{4c}$$

where η is the wave impedance of the medium. In this form, (4) can be a valuable tool in order to tackle the vectorial field shaping, as it is straightforward that the norm I becomes a function of the scalar function A_z, expressed as

$$I = f(A_z(x, y, z)). \tag{5}$$

The problem introduced in (5) presents a simpler formulation compared to the original one. In fact, given the supposed TM mode, we reduce the independent variables to one, the scalar function A_z. In contrast, in (1), the independent variables were two E_x and E_y. Besides, the procedure can be applied also to a single component, which will be the target in our case, for simplicity and to prove the concept. In addition, the z-component of the field will be considered since it is directly related to the scalar potential A_z as of (4c).

A. Presentation of the Algorithm

Given an aperture located at $z = 0$ (Fig. 1), the objective is to shape the field in the volume V, given specific requirements, either on the norm or some field components. The volume is segmented in N horizontal parallel planes, equally spaced along z-direction. The requirements are given by specific field masks, which may differ from plane to plane. The whole process can be summed as follows.

1) Calculate the field $E^n(x, y, z_n)$ for $n = 1, \ldots, N$, generated by the aperture field $E^{\text{tot}}_{\text{AP}}$.
2) Mask the field at each plane [Mask(E^n)].
3) Back-propagate each masked field to the aperture (E^n_{AP}).
4) Average all the back-propagated fields to create the new aperture distribution: $E^{\text{tot}}_{\text{AP}} = \sum_n w_n E^n_{\text{AP}}$.[1]

[1] w_n has been set to $1/N$ (unweighted sum), nevertheless other options are possible as long as $\sum w_n = 1$ [12].

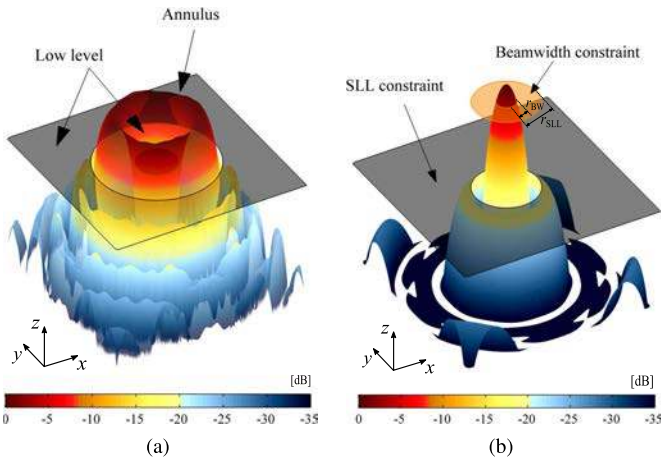

Fig. 2. 2-D mask illustrations in dB. (a) Annular mask. (b) Focusing mask.

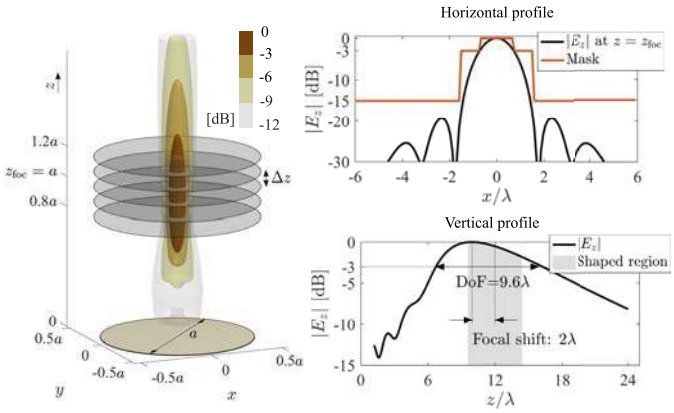

Fig. 3. 3-D focal spot shaping applied at a volume ranging from $0.8a$ to $1.2a$. The gray disks represent the shaping planes. The horizontal profile corresponds to the middle of the shaping volume ($z = z_{\text{foc}} = a$).

5) While the shaping goals are not met, repeat the process (return to step 1).

The algorithm stops if the field at step 5 lays inside the mask requirements within a certain defined error. The initial aperture distribution at step 1 can by arbitrary (e.g., a uniform one). The process is visualized in Fig. 1 in a clockwise fashion. The process is described using a scalar notation (E^n, E_{AP}, etc.), but any generalization is possible.

As already mentioned, the field manipulations are conducted using fast Fourier transforms (FFT), which allow to speed up the algorithm and to perform conveniently the "back-propagation" operation. Further information and details on these subroutines can be found in [11] and [18, p. 703] and will not be repeated here for brevity.

The key role of the procedure is played by the masking operation of step 2. The mask at each plane of the sampled volume can be the same or different, depending on the pattern requirements. For example, two different types of masks are presented in Fig. 2. In Fig. 2(a), the field is shaped into an annulus by forcing parts of it to be lower than a given threshold. This is illustrated by the transparent gray plane (including the interior circular part). Fig. 2(b) shows a "focusing" mask. It includes two basic parameters, the SLL and the beamwidth. The first one is represented by the gray plane, while the beamwidth by the orange annulus.

In more detail, the concept is to mildly alter the field's amplitude at each plane of interest, i.e., E^1, …, E^N (Fig. 1), so that it obeys the mask constraints (amplitude levels) on the considered plane. This is achieved by dumping (or amplifying) the amplitude of the field at the points that it is not laying under (or over) the given mask levels, while the phase of the field remains untouched.

For example, referring to Fig. 2(b), we identify two different levels and two different radii of interest. The gray level (SLL constraint) is a surface with a circular hole of radius r_{SLL}, while the orange level is an annulus with internal radius r_{BW} and external r_{SLL}. The SLL can be chosen to have an arbitrary level, typically lower than -10 dB below the maximum, while the beamwidth level is set to -3 dB. It is easily deduced that if the field at a given plane and at a radial distance r_{BW} is equal to -3 dB, i.e., $E(\rho = r_{\text{BW}}) = -3$ dB, the beamwidth at this plane is guaranteed to be $2r_{\text{BW}}$.

The masking process is applied iteratively between the propagation and the back-propagation steps of the algorithm, so that the aperture distribution is progressively altered and the field at the planes of interest slowly converges to the given constraints. It is evident that, in order to achieve convergence of the method, limitations exist concerning the applied constraints (i.e., too small beamwidths) and also, the masks of adjacent planes cannot differ considerably.

The aforementioned analysis has intentionally excluded any reference to a specific field component, as a result of being independent of the field component of interest. That said, either the tangential and the vertical to the aperture components can be shaped. It should also be noted that by slightly adjusting the radiation integrals, also the magnetic field can be shaped [3].

B. 3-D Focal Spot Shaping

The algorithm presented above has been exploited in a focal spot shaping scenario. The problem setup consists of an aperture that supports a radially polarized electric field (TM), but any generalization is possible. Also ϕ-symmetry is imposed, and thus the component that we aim to shape is E_z. These choices are made only to facilitate the practical implementation to follow, without affecting the proposed general approach.

Let the diameter of the aperture a be 12λ and let us try to focus the field at a distance $z_{\text{foc}} = a$. We impose a set of goals, which are a beamwidth of 1.5λ at the focal plane and an SLL of -15 dB over all the z-distances of interest. These goals are incorporated in the applied mask (Fig. 3), which will be applied to a number of planes symmetrically positioned around the targeted focal distance z_{foc}.

In the first case to examine, we shape the field in a volume that extends from $z = 0.8a$ to $z = 1.2a$ at discrete planes separated by $\Delta z = 1.2\lambda$. The result of applying our algorithm to this volume is illustrated in Fig. 3. Specifically, a 3-D representation of the distribution of E_z is provided,

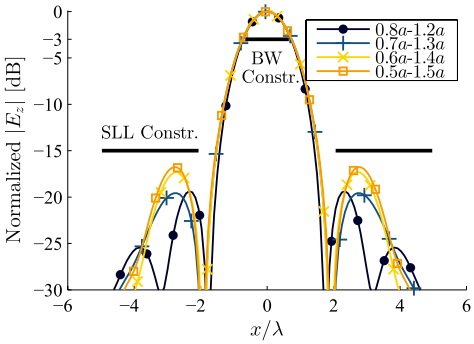

Fig. 4. E_z along x-axis at $z = 1a$ for the four different 3-D-shaped volumes.

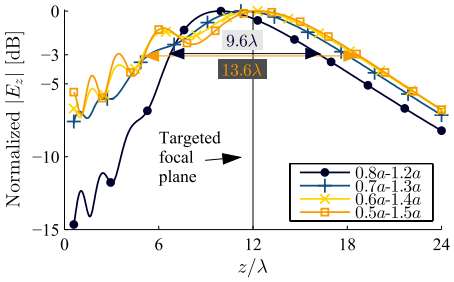

Fig. 5. E_z over z-axis for the four different 3-D-shaped volumes.

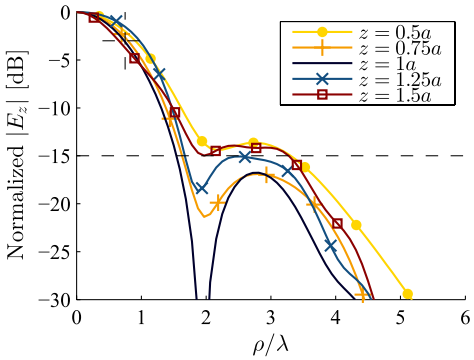

Fig. 6. E_z at various z-distances for the 3-D shaping case of 0.5a-1.5a.

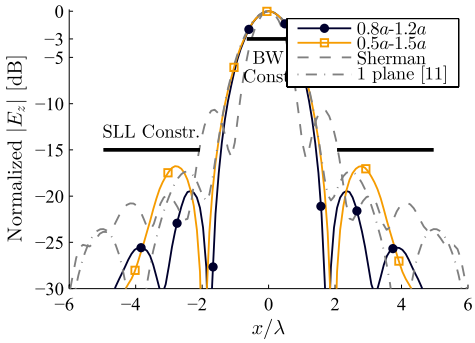

Fig. 7. Horizontal field profile computed for different focusing techniques at $z = 1a = 12\lambda$.

accompanied with the field profiles along x- and z-axes. We can observe the achieved FoMs (beamwidth, DoF, etc.). In the horizontal direction, the goals are met, nevertheless, in the vertical direction, we notice the appearance of a focal shift. In order to tackle this problem, we increase the number of shaping planes (increase the shaping volume), always symmetrically around the targeted focal distance.

Three additional shaping volumes, centered at $z = a$, have been considered, namely, between 0.7a-1.3a, 0.6a-1.4a, and 0.5a-1.5a. In all cases $\Delta z = 1.2a$. Fig. 4 shows the behavior of E_z at $z = a$ for all four shaping volumes. We observe that both the beamwidth and the SLL constraints are respected for all four shaping cases. This shows the capability of our technique to control the field shape in the transverse-to-the-aperture direction.

However, the greatest advantage of the proposed scheme is the capability to control the field also in the normal-to-the-aperture direction. This can be observed in Fig. 5, where the behavior of E_z over z-axis is illustrated for the four shaping cases. We can notice the gradual decrease of the focal shift as the shaping volume increases. In addition, it is possible to appreciate the capability of the proposed approach to shrink and expand the DoF. Specifically, we observe a DoF of 9.6λ and 13.6λ when the shaping volume ranges between 0.8a and 1.2a and between 0.5a and 1.5a, respectively. The initial aperture distribution for all the cases has been a uniform one, and typically 20 iterations are enough to reach the shaping goals within the accepted error.

Finally, the horizontal profiles of the last and most demanding shaping case (0.5a-1.5a) at various z-distances are presented in Fig. 6. The applied mask is also provided as a reference (black dashed lines symbolize the SLL and beamwidth criterion). We notice that the curves at the extremities of the shaping volume (0.5a and 1.5a) appear to have slightly higher SLL (-14 dB) than the initial constraint of -15 dB. This is an unavoidable issue, which, however, allows the convergence of the algorithm within a given percent of error [12].

C. Assessment of the Proposed Technique

In order to assess the performance of the proposed technique, we compare the achieved focal characteristics for different focusing methodologies. The aperture characteristics are the same as the ones applied above for 3-D shaping (TM polarized, diameter $a = 12\lambda$, $z_{\text{foc}} = a$).

The first approach considered is the one proposed in [4]. In the latter, a quadratic phase taper is imposed on the aperture field distribution to focus the field in the Fresnel zone (gray dashed lines in Figs. 7 and 8). In particular, this theory [4] concerns linearly polarized apertures and field components that are transverse to the aperture. In our case—TM polarization and shaping of E_z—it results in a significant focal shift (3.5λ). This is illustrated in Fig. 8. Besides, the beamwidth and SLL of the radiated field cannot be arbitrarily defined (Fig. 7).

It is apparent that the aforementioned focal shaping technique cannot serve situations where precision is required. This has been tackled in [11], where a novel approach to 2-D shaping was introduced, capable of shaping the field

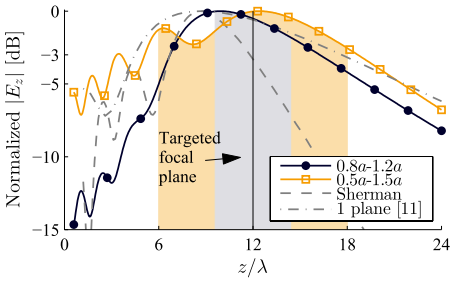

Fig. 8. E_z over z-axis for various focusing schemes. The colored areas mark the shaped regions for the included 3-D shaped cases.

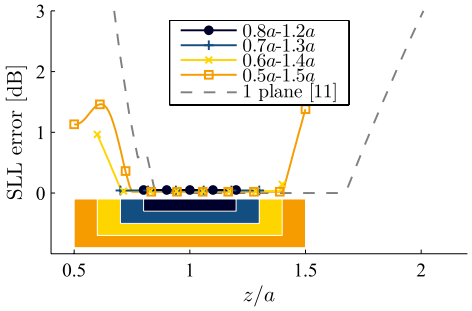

Fig. 9. SLL qualitative study. The colorful regions represent the z-distances over which each case is shaped. The diameter of the aperture is $a = 12\lambda$.

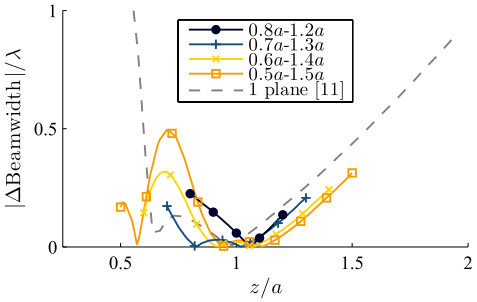

Fig. 10. Deviation of the beamwidth from the nominal mask constraint of 1.5λ for the 3-D and 2-D shaping.

along one transverse-to-the-aperture plane. This case is represented with the gray dashed-dotted lines in Fig. 7 and shows excellent control over the beamwidth and the SLL constraints. Nevertheless, this technique lacks control over the focal distance and the DoF, as clearly shown in Fig. 8. In fact, the DoF, which is 11.7λ in the presented case (Fig. 8), is a noncontrollable quantity, while the focal shift is around 4λ. This stems from the fact that shaping a given plane ($z_{\text{foc}} = a$ in this case) cannot guarantee that this plane will also be the focal one.

The novelty presented in this paper can tackle this lack of precision by applying a given focusing mask not on one, but on multiple planes. This provides the capability to control also the DoF and to predict the focal distance with superior accuracy. Consequently, by applying the same focusing mask at a varying number of planes, centered around the requested focal plane, we have succeeded in modifying the focal characteristics also along the normal direction to the radiating aperture.

This can be observed in Fig. 8, where the two marginal 3-D shaping cases (0.8a-1.2a and 0.5a-1.5a) are compared to the other shaping techniques. When it comes to the 3-D shaped fields, we notice the wide modification of the DoF between the two cases, while maintaining the focal shift at a minimum level. Specifically, in the first case the focal shift is lower than 3λ, while in the second one it remains in the order of magnitude of a fraction of the wavelength (0.4λ). Moreover, the control of the DoF is significant. In fact we observe a 9.6λ and 13.6λ DoF for the two cases (see Fig. 5), which, compared to the one-plane shaped field (DoF of 11.7λ), correspond to 18% and 16% shrink and expand ratio, respectively. These two examples also show that a better control of the focal shift is achieved for larger shaping volumes, for which the constraints of the NF are more smoothly imposed.

A qualitative study has also been carried out in order to assess the advantages and the superiority of the proposed technique compared to its 2-D predecessor [11]. In Fig. 9, we observe a comparison of the four shaping cases with [11], in terms of the achieved SLL behavior. The SLL for the transverse to the aperture profile of E_z along z-axis is calculated and illustrated within the shaping area along z. The error denotes dBs higher than the original requirement of -15 dB. We notice that for the two first cases (smaller volumes, 0.8a-1.2a and 0.7a-1.3a) the mask requirement is respected completely and thus the error is zero. For the other two cases (larger volumes, 0.6a-1.4a and 0.5a-1.5a), the error, that appears only at the extremities of the volume, remains lower than 1.5 dB from the requirements. On the contrary, in the case of 2-D shaping, we notice that despite the fact that the region where the SLL is lower than -15 dB might be large, it remains uncontrolled and definitely more unbalanced compared to the 3-D shaping scenario.

Another comparison concerns the behavior of the beamwidth along the shaping volume, which is presented in Fig. 10. In this case, we observe the absolute deviation of the beamwidth from the original mask requirement of 1.5λ. Of course, we are not expecting to achieve a constant beamwidth, since that would signify that we are dealing with nondiffractive beams/waves, which is not our case. Nevertheless, we can appreciate the much more stable behavior of the 3-D-shaped fields, which do not deviate (in the worst case) more than 0.5λ, in contrast to the much more unbalanced 2-D-shaped field.

It appears that the more planes are shaped, alternatively, the more constraints are applied, and the SLL eventually rises. This is not surprising since the number of degrees of freedom [19], [20] for a given field is bounded.

It is important to say that the frequency of operation is intentionally left undetermined, since the theoretical developments presented are independent of the frequency. This provides inherent frequency scalability to the results. Needless to say that also the electrical size of the aperture can be arbitrarily chosen.

TABLE I

RLSA SIZES: l_t IS THE RADIUS AND ρ_t THE LENGTH OF THE SLOTS OF EACH RING

Ring Number	1	2	3	4	5	6	7	8	9	10
l_t [mm]	1.94	2.61	2.99	3.11	3.09	3.17	3.17	3.09	4.2	2.81
ρ_t [mm]	5.2	11.36	17.39	23.46	29.59	34.55	40.42	46.49	50.39	57.99

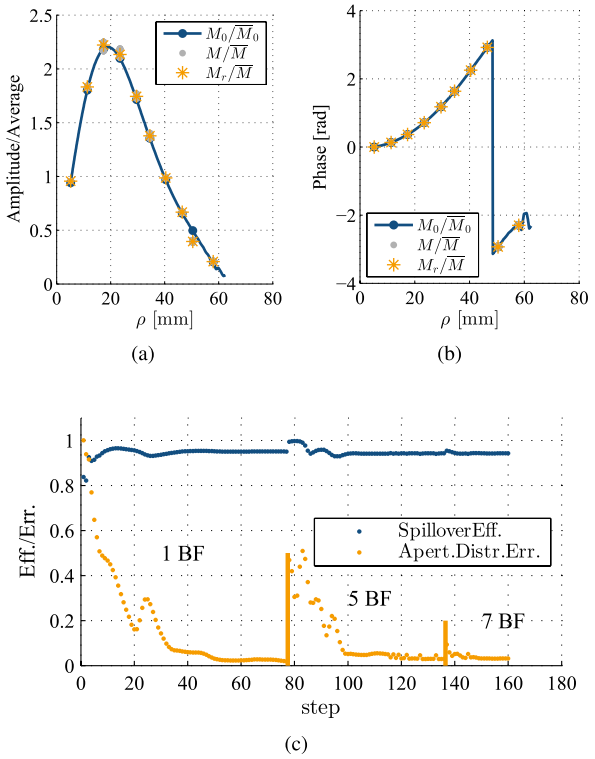

Fig. 11. Mapping of the aperture distribution to the RLSA. (a) Amplitude. (b) Phase. (c) Achieved efficiency and error. $M_0/\overline{M}_0$, $M/\overline{M}$, and $M_r/\overline{M}$ stand for the magnetic current distribution derived by the theoretical modeling, the magnetic current of each slot, and the averaged magnetic current of each ring, respectively. BF represents the number of entire domain basis functions utilized by the MoM tool. The spillover efficiency is calculated as the percentage of power reaching the edge of the aperture over the total injected power.

III. RLSA DESIGN

To experimentally validate the proposed concept, an RLSA has been designed, manufactured, and measured at 30 GHz. The diameter of the antenna is $a = 12\lambda$ (12 cm at 30 GHz), in accordance with the previously reported theoretical developments.

The RLSA structure is designed to synthesize the aperture field corresponding to the case of shaping the planes ranging from $0.5a$ to $1.5a$. This electric field distribution is ϕ-symmetric, and due to the mode that is assumed (TM_0), it is radially polarized ($\mathbf{E}_{\mathrm{AP}} = E_\rho(\rho)\hat{\boldsymbol{\rho}}$). It can be easily translated to equivalent magnetic currents, which in our case are calculated as $\boldsymbol{M} = -\hat{\boldsymbol{n}} \times \mathbf{E}_{\mathrm{AP}} = M_0(\rho)\hat{\boldsymbol{\phi}}$.

The obtained magnetic current distribution (M_0) to synthesize is demonstrated in Fig. 11(a) and (b), where its amplitude and phase distribution are presented, respectively. An optimization procedure is launched, which derives the radii (ρ_t) and lengths (l_t) of each ring of slots (Fig. 13) that will generate a sampled version M of the original continuous magnetic current distribution M_0. The slots of each ring have the same length.

An in-depth presentation of the optimization and synthesis procedure can be found in [21]. In particular, the equivalent magnetic dipole moment of each slot $M/\overline{M}$ ($\overline{M}$ stands for the average) is calculated using an in-house MoM tool [22], [23]. The calculated magnetic dipole moments are compared to the reference ones $M_0/\overline{M}_0$. These are shown in Fig. 11(a) and (b). Besides, the etching precision of the fabrication process is respected for the minimum features and distance amongst patterns.

The optimization results for the RLSA synthesis are given in Fig. 11(c), where a very good agreement (error $< 4\%$) and a very high spillover efficiency (94%) are observed. The final slot positions and lengths are included in Table I. The slot width w is set to $\lambda_d/10 = 0.67$ mm, where λ_d is the effective wavelength inside the dielectric substrate.

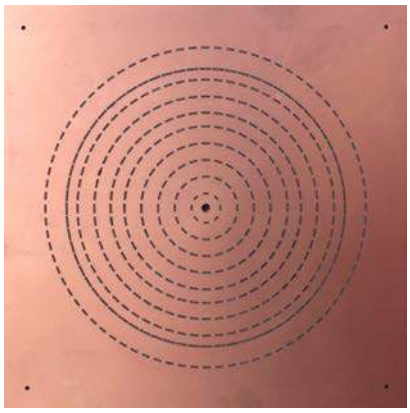

Fig. 12. Top view of the manufactured antenna.

IV. PROTOTYPING

The design approach presented in Sections II and III is here validated by the proposed RLSA structure. The resulting antenna, which can be seen in Fig. 12, was manufactured on a Rogers RT/duroid 5880 substrate with $\varepsilon_r = 2.2$ and thickness $h_s = 2.54$ mm using laser ablation. The structure is centrally fed using a coaxial probe (internal and external diameter: 0.635 and 1.46 mm, respectively) which is attached to the back side of the structure with a coaxial connector (SRI 25-130-1000-90). The matching of the antenna to the connector is achieved by a metallic disk connected to the feeding probe, as illustrated in Fig. 13, where the various sizes measure $r_1 = 1.4$ mm and $h_1 = 1.54$ mm. A -10 dB matching is achieved over a 2.5% bandwidth, as shown in Fig. 14. In addition, good agreement between measurement and full-wave simulation (HFSS) can be recognized.

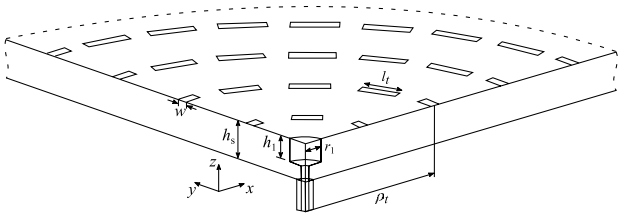

Fig. 13. Truncated one quarter of the antenna.

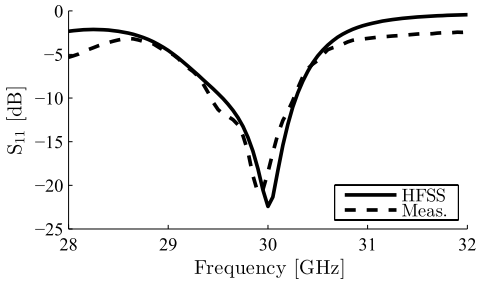

Fig. 14. Reflection coefficient of the manufactured antenna.

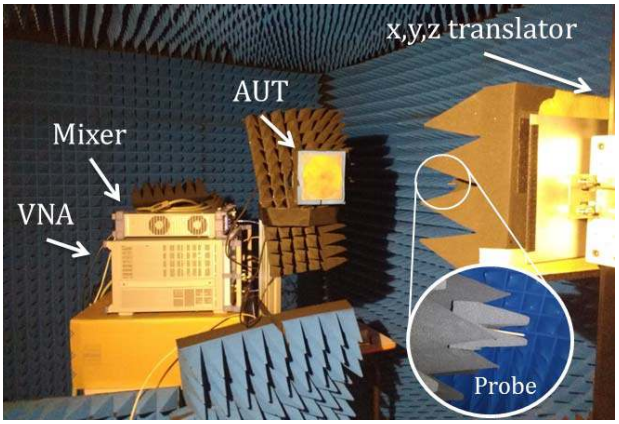

Fig. 15. Picture of the measurement setup. VNA and AUT stand for vector network analyzer and antenna under test, respectively.

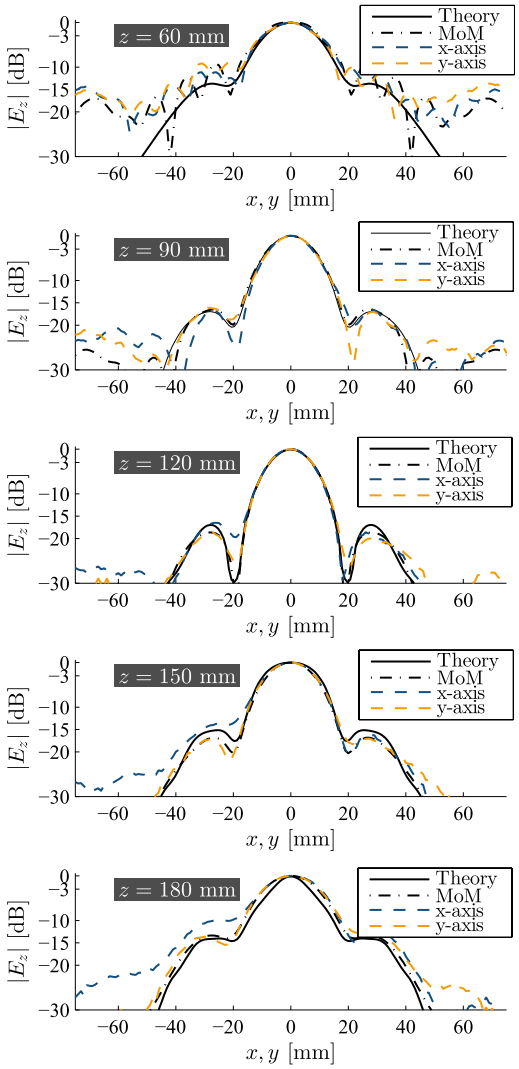

Fig. 16. Measurements versus theory (continuous aperture) and simulation (MoM) of the normalized E_z (30 GHz) at five different distances from the antenna, namely, 60, 90, 120, 150, and 180λ. The central distance coincides with the focal one.

The E_z component of the NF of the antenna was measured at the NF test range of IETR using an NF probe made by a semirigid UT-85 coaxial cable with the internal conductor exposed at the end for a distance of $\lambda/10$ (λ is the freespace wavelength at the operating frequency). The measurement setup can be visualized in Fig. 15.

The NF radiated by the structure was measured over an area of 150×150 mm^2 with a step of 1 mm ($\lambda/10$ at $f_0 =$ 30 GHz) at different distances from the RLSA aperture, namely, 60, 90, 120, 150, and 180 mm. The results can be observed in Fig. 16 for all the aforementioned distances. The agreement with the MoM results and the theory is excellent. The curves denoted as "theory" stand for the results obtained by the continuous aperture modeling and concern the output of the optimization process (shaping between $0.5a$ and $1.5a$).

A minor disagreement appears along the x-axis, due to a small manufacturing default. Specifically, in order to realize the matching disk at the center of the antenna, the substrate is drilled to a depth of h_1 (Fig. 13) and then copper plated. A final thickness of few micrometers is expected to be deposited. Unfortunately, part of this copper sheet was removed during the soldering of the connector.

Another possible source of the minor disagreements could be the mechanical stability of the measuring probe. The latter is provided only by the stiffness of the semirigid coaxial cable. Small perturbations of the orientation of the pin can result in asymmetries of the measured field. An additional possible reason originates from the edge effects. Despite the high spillover efficiency, some energy still arrives at the edge of the structure, resulting in spurious radiation. This has not been accounted for in the simulation, where infinite metallic plates are considered. Last but not least, the etching accuracy of the radiating slots could result in a slightly perturbed aperture distribution compared to the ideal one.

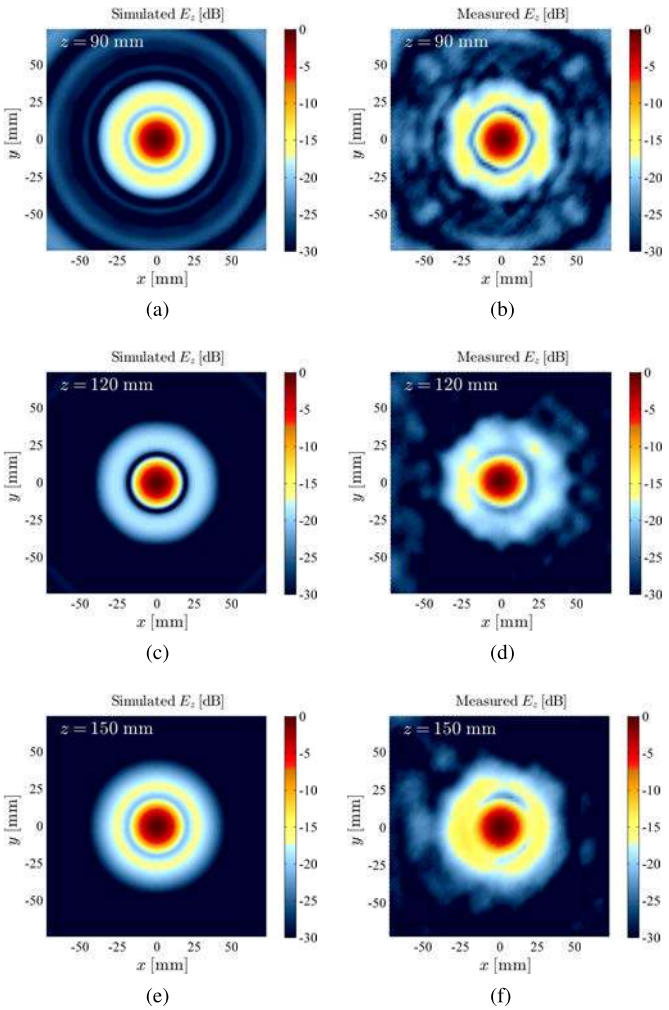

Fig. 17. 2-D illustrations of the normalized E_z at three different heights (90, 120, and 150 mm). (a), (c), and (e) Simulations. (b), (d), and (f) Measurements.

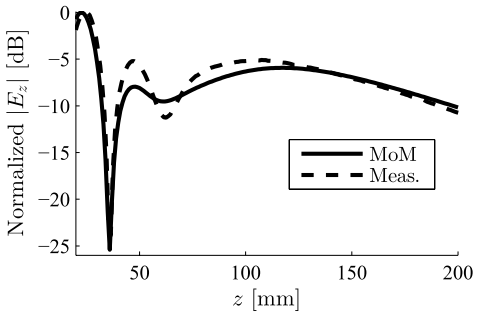

Fig. 18. Measurement at 30 GHz versus simulation of E_z over the z-axis.

Further 2-D illustrations of the field are presented in Fig. 17. Three horizontal cuts at different distances from the structure are shown and compared with their equivalent simulation data (left). The agreement is considered good, with the symmetry of the patterns being very satisfying.

Another important graph is presented in Fig. 18. This figure shows the behavior of E_z along the z-axis. The agreement

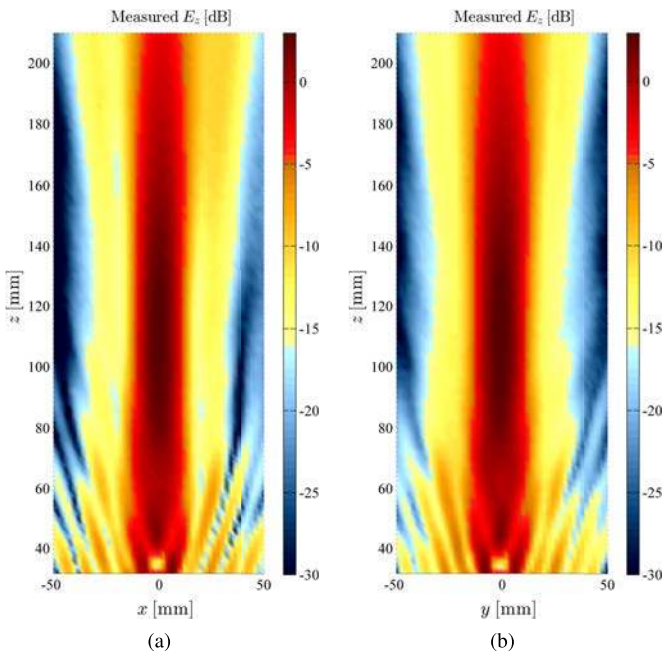

Fig. 19. Measured E_z (normalized) at 30 GHz, on the (a) $y = 0$ and (b) $x = 0$ plane.

with the simulation results is very good despite the minor shift of the maximum. Finally, and in order to present a complete picture of the measurements, two vertical cuts (xz- and yz-planes) are illustrated in Fig. 19. We can appreciate the smooth behavior of the field along the shaped volume, validating the overall design approach.

V. Conclusion

The focal characteristics of a focusing aperture have been shaped in the NF according to a defined mask within a 3-D volume using an iterative algorithm. The capability of the proposed technique to shape a focal volume at will was illustrated, setting a starting point toward high accuracy 3-D shaping. Different focal depths have been achieved while maintaining the spot diameter unchanged and with minimal translation of the focal plane. This is an important improvement with respect to the currently used design techniques for focusing systems in the NF. Four different cases have been examined, with one being tested also experimentally. In particular, an RLSA with constrained NF at 30 GHz was manufactured and measured. The measurements show very good agreement with the simulation data from an in-house MoM code and theory, validating the proposed design procedure. It should be noted that the proposed shaping approach is versatile and could be applied also in different field-shaping scenarios with the appropriate modifications (e.g., magnetic field shaping [24]). Potential applications range from wireless power transfer to mine detection and medical imaging.

Acknowledgment

The authors would like to thank Dr. L. Le Coq for his precious help and support during measurements.

REFERENCES

[1] K. D. Stephan, J. B. Mead, D. M. Pozar, L. Wang, and J. A. Pearce, "A near field focused microstrip array for a radiometric temperature sensor," *IEEE Trans. Antennas Propag.*, vol. 55, no. 4, pp. 1199–1203, Apr. 2007.

[2] D. A. M. Iero, L. Crocco, and T. Isernia, "Thermal and microwave constrained focusing for patient-specific breast cancer hyperthermia: A robustness assessment," *IEEE Trans. Antennas Propag.*, vol. 62, no. 2, pp. 814–821, Feb. 2014.

[3] S. Kim, J. S. Ho, and A. S. Y. Poon, "Wireless power transfer to miniature implants: Transmitter optimization," *IEEE Trans. Antennas Propag.*, vol. 60, no. 10, pp. 4838–4845, Oct. 2012.

[4] J. Sherman, III, "Properties of focused apertures in the Fresnel region," *IRE Trans. Antennas Propag.*, vol. 10, no. 4, pp. 399–408, Jul. 1962.

[5] A. Buffi, P. Nepa, and G. Manara, "Design criteria for near-field-focused planar arrays," *IEEE Antennas Propag. Mag.*, vol. 54, no. 1, pp. 40–50, Feb. 2012.

[6] Y. Li and E. Wolf, "Focal shifts in diffracted converging spherical waves," *Opt. Commun.*, vol. 39, no. 4, pp. 211–215, Oct. 1981.

[7] I.-H. Lin, C. Caloz, and T. Itoh, "Near-field focusing by a nonuniform leaky-wave interface," *Microw. Opt. Technol. Lett.*, vol. 44, no. 5, pp. 416–418, Mar. 2005.

[8] J. L. Gomez-Tornero, A. R. Weily, and Y. J. Guo, "Rectilinear leaky-wave antennas with broad beam patterns using hybrid printed-circuit waveguides," *IEEE Trans. Antennas Propag.*, vol. 59, no. 11, pp. 3999–4007, Nov. 2011.

[9] D. Blanco, J. L. Gomez-Tornero, E. Rajo-Iglesias, and N. Llombart, "Radially polarized annular-slot leaky-wave antenna for three-dimensional near-field microwave focusing," *IEEE Antennas Wireless Propag. Lett.*, vol. 13, pp. 583–586, 2014.

[10] Q. Zhan, "Cylindrical vector beams: From mathematical concepts to applications," *Adv. Opt. Photon.*, vol. 1, no. 1, pp. 1–57, Jan. 2009.

[11] M. Ettorre *et al.*, "On the near-field shaping and focusing capability of a radial line slot array," *IEEE Trans. Antennas Propag.*, vol. 62, no. 4, pp. 1991–1999, Apr. 2014.

[12] R. Piestun and J. Shamir, "Synthesis of three-dimensional light fields and applications," *Proc. IEEE*, vol. 90, no. 2, pp. 222–244, Feb. 2002.

[13] M. Zamboni-Rached, "Stationary optical wave fields with arbitrary longitudinal shape by superposing equal frequency Bessel beams: Frozen waves," *Opt. Exp.*, vol. 12, no. 17, pp. 4001–4006, Aug. 2004.

[14] Z. Bouchal and J. Wagner, "Self-reconstruction effect in free propagation of wavefield," *Opt. Commun.*, vol. 176, nos. 4–6, pp. 299–307, Apr. 2000.

[15] J. Rosen and A. Yariv, "Synthesis of an arbitrary axial field profile by computer-generated holograms," *Opt. Lett.*, vol. 19, no. 11, pp. 843–845, Jun. 1994.

[16] G. Bellizzi and O. Bucci, "Blind focusing of electromagnetic fields in hyperthermia exploiting target contrast variations," *IEEE Trans. Biomed. Eng.*, vol. 62, no. 1, pp. 208–217, Jan. 2015.

[17] J. J. Stamnes, *Waves in Focal Regions: Propagation, Diffraction and Focusing of Light, Sound and Water Waves*. Boca Raton, FL, USA: CRC Press, Jan. 1986.

[18] C. A. Balanis, *Antenna Theory: Analysis and Design*. Hoboken, NJ, USA: Wiley, 2005.

[19] O. M. Bucci and G. Franceschetti, "On the spatial bandwidth of scattered fields," *IEEE Trans. Antennas Propag.*, vol. 35, no. 12, pp. 1445–1455, Dec. 1987.

[20] M. Casaletti, S. Maci, and G. Vecchi, "A complete set of linear-phase basis functions for scatterers with flat faces and for planar apertures," *IEEE Trans. Antennas Propag.*, vol. 59, no. 2, pp. 563–573, Feb. 2011.

[21] M. Albani, A. Mazzinghi, and A. Freni, "Automatic design of CP-RLSA antennas," *IEEE Trans. Antennas Propag.*, vol. 60, no. 12, pp. 5538–5547, Dec. 2012.

[22] M. Casaletti, R. Sauleau, M. Ettorre, and S. Maci, "Efficient analysis of metallic and dielectric posts in parallel-plate waveguide structures," *IEEE Trans. Microw. Theory Techn.*, vol. 60, no. 10, pp. 2979–2989, Oct. 2012.

[23] M. Casaletti, G. Valerio, J. Seljan, M. Ettorre, and R. Sauleau, "A full-wave hybrid method for the analysis of multilayered SIW-based antennas," *IEEE Trans. Antennas Propag.*, vol. 61, no. 11, pp. 5575–5588, Nov. 2013.

[24] A. Grbic, R. Merlin, E. M. Thomas, and M. F. Imani, "Near-field plates: Metamaterial surfaces/arrays for subwavelength focusing and probing," *Proc. IEEE*, vol. 99, no. 10, pp. 1806–1815, Oct. 2011.